

Timepix3: single-pixel multi-hit energy-measurement behaviour

Hubertus Bromberger^a,^b,^c David Pennicard,^b Rafael Ballabriga,^c Sebastian Trippel^b^{a,d,1,*} and Jochen Küpper^b^{a,d,e}

^aCenter for Free-Electron Laser Science CFEL, Deutsches Elektronen-Synchrotron DESY, Notkestr. 85, 22607 Hamburg, Germany

^bDeutsches Elektronen-Synchrotron DESY, Notkestr. 85, 22607 Hamburg, Germany

^cExperimental Physics Department, CERN, Meyrin, 1211, Switzerland

^dCenter for Ultrafast Imaging, Universität Hamburg, Luruper Chaussee 149, 22761 Hamburg, Germany

^eDepartment of Physics, Universität Hamburg, Luruper Chaussee 149, 22761 Hamburg, Germany

E-mail: sebastian.trippel@cfel.de

ABSTRACT: The event-driven hybrid-pixel detector readout chip, Timepix3, has the ability to simultaneously measure the time of an event on the nanosecond timescale and the energy deposited in the sensor. However, the behaviour of the system when two events are recorded in quick succession of each other on the same pixel was not studied in detail previously. We present experimental measurements, circuit simulations, and an empirical model for the impact of a preceding event on this energy measurements, which can result in a loss as high as 70%. Accounting for this effect enables more precise compensation, particularly for phenomena like timewalk. This results in significant improvements in time resolution — in the best case, multiple tens of nanoseconds — when two events happen in rapid succession.

KEYWORDS: Hybrid detectors; Instrumentation and methods for time-of-flight (TOF) spectroscopy

ARXIV EPRINT: [2403.07184](https://arxiv.org/abs/2403.07184)

*Corresponding author.

¹Website: <https://www.controlled-molecule-imaging.org>.

Contents

1	Introduction	1
2	Methods	3
2.1	Experimental setup	3
2.2	Circuit model	4
2.3	Detector simulation	4
3	Results and discussion	5
3.1	Experimental results	5
3.2	Detector simulation	6
3.3	Loss model	9
4	Conclusions	10

1 Introduction

In the rapidly evolving field of scientific and industrial imaging, there is an ever-increasing need for detectors capable of sensing individual events with high temporal and spatial resolution, while being able to cope with high event rates [1–4]. Such detectors have a broad range of applications, including nuclear medicine, high-speed industrial inspection, particle and atomic, molecular, and optical (AMO)-physics experiments [5–11]. In addition to single-event time and location determination, its energy deposited in the sensor is also an important aspect. Particularly, in AMO physics, the precise measurement of the charged-particle time-of-flight is imperative for ionic fragments identification and the 3D momentum vector determination — both relevant for chemical dynamics studies [12, 13]. Furthermore, in the context of Bragg peak recognition for proton therapy, energy measurement makes it possible to identify the energy deposition profile of protons, a key factor in dose delivery [8, 9, 14]. In the realm of high-energy physics, energy data can indicate the number of particles striking the detector simultaneously, contributing to particle identification and event reconstruction [4, 15–17]. Additionally, for astrophysics applications, the brightness of events such as gamma bursts or while monitoring space weather, is invaluable to determine the nature of the phenomena under investigation [18].

However, the question remains whether one can still accurately determine events when two or more occur within a short period of time. This is particularly pertinent for AMO, high-energy physics and radiation therapy applications, where high-intensity, high-frequency events are commonplace [4, 14, 19]. Here, the detector’s ability to accurately measure and differentiate between rapid, successive events becomes crucial.

The Medipix collaboration has developed the Timepix line of hybrid-pixel detectors [20–22]. These detectors, such as the current Timepix3 and Timepix4 models, offer high spatial and temporal resolution, a low mass, low-power usage, high radiation tolerance as well as the possibility to be used with visible photons [1, 22–24]. In this regard, the versions for visible light have the great advantage that large-area detectors can be imaged onto the camera chip using optical methods. Additionally,

with the help of image intensifiers, a single photon sensitivity can be achieved, important for instance for neutrino experiments [25]. In general, all these detectors can measure single particles at low noise and with a high dynamic range. They can time stamp these events by time-of-arrival (ToA) at a resolution from 1.6 ns down to only hundreds of picoseconds. In addition, the amplifier is designed such that the duration of the pulse produced by a hit is proportional to the energy deposited in the sensor and thus, by measuring the duration of the pulse (time over threshold, ToT) the deposited energy can be approximated [20, 22, 26].

The Timepix3 chip handles multiple consecutive events, illustrated in the upper row in figure 1, in three distinct ways depending on the timing of the incoming events [20], depicted in the lower row of figure 1. In figure 1 b, the second event arrives during the readout time of the first event and, therefore, is discarded and only the first event is recorded. Figure 1 a shows the case when the second event arrives within the ToT of the first event or within 25 ns after the signal from the first event went below the threshold. This results in a single detector event for which, due to analogue pile up, the measured ToT is approximately the sum of the ToTs of the individual events, as illustrated in figure 1 a. In the third scenario the second event arrives after the readout time of the first event is completed; both are recorded as separate events. The expected ToT distribution for equal intensities in both events is illustrated in the lower row and should consist of two hits with similar ToT values provided the two events have the same amplitude.

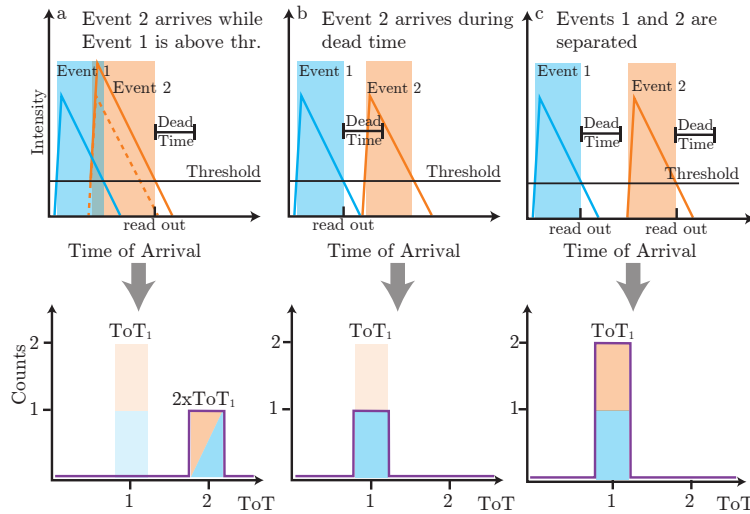


Figure 1. Sketch of event processing in Timepix3. The top row presents an illustration of two events impinging on a detector pixel at different times. Their resulting energy (ToT) histograms are drawn in the second row, indicated by the purple line. The darker colour represents the actual measured events, whereas the lighter colour indicates lost histogram events.

Here, we report measurements on the influence of preceding pulses on the energy recorded, which demonstrate an influence for pulse-to-pulse separations up to $\sim 10 \mu\text{s}$. Following a brief description of our experimental setup, we present our experimental results from a systematic study of the Timepix3 response to a second event in a single pixel within a few microseconds. We propose an explanation for the observed effect, yielding a predictive model for Timepix3 that could be used to correct the observed effect in post-analysis.

2 Methods

2.1 Experimental setup

The experimental setup is illustrated in figure 2. Two super-bright light-emitting diodes (LEDs), are mounted next to each other facing a thin entrance window, visible light-sensitive 300 μm -thick p -on- n silicon sensor biased with 50 V, bonded to Timepix3 [24, 27]. The camera objective is slightly out of focus to have the resulting images of the two LEDs slightly overlap on the sensor. A delay generator (Stanford Research DG645) was used to control the signal amplitude and relative delay of the LEDs. The delay generator was set to internal trigger mode at a repetition rate of 100 Hz. The reference output channel of the delay generator is used as a trigger-input signal for the Timepix3 camera.

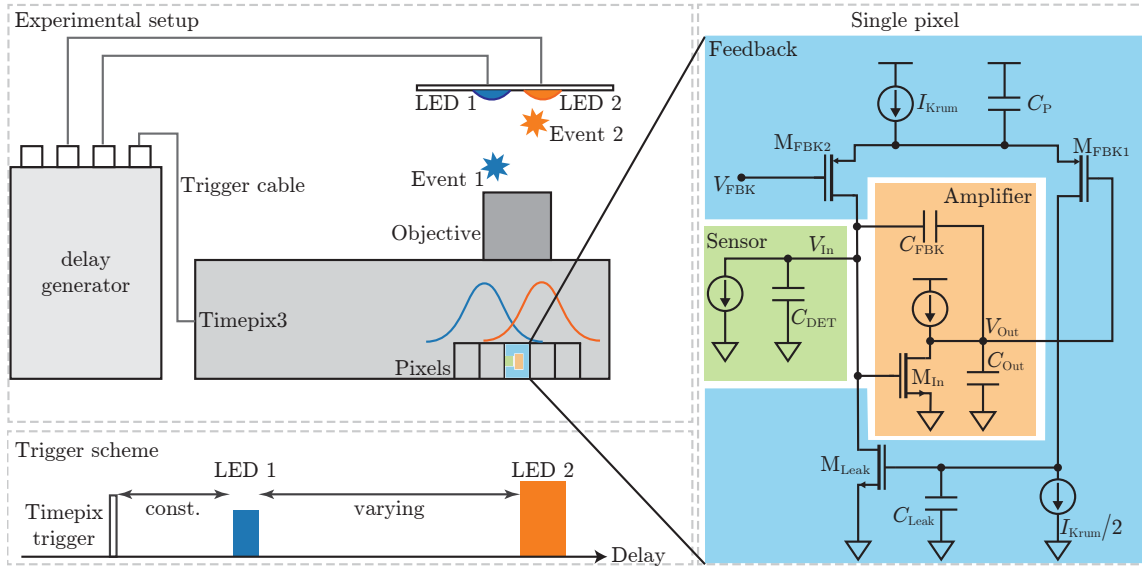


Figure 2. Schematic of the experimental setup, the trigger scheme, and a single pixel circuit: the left upper part depicts the experimental setup with the Timepix3 camera facing two LEDs controlled for intensity and delays by a delay generator. The lower left part depicts the trigger scheme for the camera and LEDs, respectively. The height and width of the vertical boxes illustrate the control of the illumination for the respective LEDs by controlling the widths and amplitudes of the driver pulses. The right shows an illustration of a simplified schematic from a single pixel of the Timepix3-front-end amplifier, highlighting the equivalent small signal circuit model of a sensor (green), an amplifier circuit based on a cascoded common source transistor (orange), and the feedback reset path (blue). Currents, voltages, and capacitances are labelled by I , V , C and transistors as M .

To independently control the intensity and delay of the LEDs, each LED was connected to a separate output channel of the delay generator. To operate the LEDs within a ToT range of 0.1–2 μs , the channel level and pulse width were adjusted, as indicated in the lower part of figure 2, between 2...5 V and 15...50 ns, respectively. For the smaller ToT the voltage was adjusted at a constant pulse duration of 15 ns until the desired ToT was reached. All other ToTs were adjusted by picking the corresponding pulse duration at a channel level of 5 V. All pulse durations applied were still short enough for the relevant timescales of the experiment, e.g., some μs . For the delay scans, LED 1 was kept at a fixed delay with respect to thereference trigger and the delay of LED 2 was swept.

The adjustable reference current I_{Krum} in the Timepix3 chip that controls how quickly the amplifier output voltage in a pixel returns to its baseline value after charge is deposited was set to

$I_{\text{Krum}} = 10$ steps; 1 step for the digital-to-analogue converter corresponds to 0.24 nA. The data was recorded for 15 s, corresponding to 1500 event pairs, at each delay point. Additionally, all pixels but one were electronically masked on the Timepix3 hardware. We carefully tested that the masking does not influence the dynamics described below and is not influenced by effects that might be related to synchronous illumination of a large fraction of the pixels in the matrix. The hardware was controlled using PymePix [28, 29] with Tango [30].

To eliminate the possibility of the LEDs themselves being the source of the demonstrated behaviour, we also performed independent measurements of the brightness of the two LEDs with a photodiode (Thorlabs, DET10). Here, the light of the LEDs was focused with a 25 mm focal length lens onto the photodiode, the signal was amplified with a transimpedance amplifier (Femto, HVA-500M-20-B) and recorded by a digitizer (SPDevices ADQ14). The amplitude of the second LED was constant within the error of the measurement and did not depend on delay, see figure S1.

2.2 Circuit model

To conceptionally understand the dynamics of a single Timepix3 pixel, it is required to look into its electronics. A Timepix3 pixel contains only a charge-sensitive preamplifier (CSA) followed by a discriminator, without a shaping amplifier. This enables ToT measurements relying on a pulse duration that linearly increases with energy. The pulse is shaped by the transfer function of the charge sensitive amplifier [7]. A schematic of the CSA circuit is provided in the right part in figure 2. It illustrates (1) the equivalent small signal circuit model of a sensor (green), (2) a simplified amplifier circuit based on a cascoded common source transistor (M_{In}) (orange), and (3) the feedback reset path (blue). The feedback reset path is based on the Krummenacher architecture [31], and it implements two functions. The first function is to discharge the feedback capacitor (C_{FBK}) with a constant current after the charge delivered by the sensor has been integrated. Since the discharge rate is constant, it results in a ToT that is almost linearly proportional to the deposited charge. This function is performed by the transistors M_{FBK1} and M_{FBK2} that, together with the tail-current source I_{Krum} , form a differential-pair structure. The second function is to compensate for the leakage current produced by the sensor, which can vary over time. The circuit can react to changes in leakage current at frequencies up to ~ 100 kHz, though usually the natural drifts occur more slowly than this. The leakage-current-compensation network is, therefore, a low-pass frequency circuit in a feedback path whose purpose is to filter the very low frequency components of the signal delivered by the sensor, i.e., the leakage current. The single pixel circuit diagram includes C_{FBK} and C_{Leak} as real capacitance components. C_{Leak} is usually chosen on the order of hundreds of femto farads. The remaining capacitors model equivalent or parasitic capacitances intrinsic to the electronics.

2.3 Detector simulation

A simulation of the pixel response was made using Cadence Virtuoso [32] based on the circuit shown in figure 2. Figure 3 shows the output voltage V_{Out} of the amplifier following an input pulse of 5000 electrons delivered within a time period much shorter than any timescale relevant for the chip dynamics [7]. The sensor exhibits a positive polarity and a positive flow of charge into the CSA, which results in a negative-going output pulse at V_{Out} . Changes in V_{Out} will be accompanied by a corresponding change in V_{In} , with the latter having opposite polarity and much smaller magnitude. When the current pulse arrives, there is a rapid initial voltage decrease (increase) within the first

50 ns for V_{Out} (V_{In}). Following this, there is a linear increase (decrease) in V_{Out} (V_{In}), due to the linear discharge of the capacitor C_{FBK} through the feedback circuit. The duration of the linear V_{Out} increase is proportional to the magnitude of the input electron pulse. This voltage is subsequently recorded by the discriminator to determine the ToT. The discharge process spans approximately $1.4 \mu\text{s}$, designated as region 1 (blue area), exhibits damped oscillations in region 2 (red), and concludes slightly above V_{Out} around $2.7 \mu\text{s}$, marking the onset of an exponential decay toward the initial voltage in region 3 (green); V_{Out} converges with a time constant of $12.3 \mu\text{s}$.

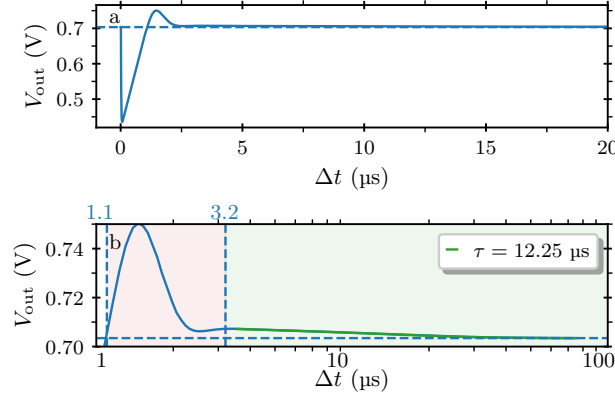


Figure 3. (a) Response of the circuit to a 5000 electrons input impulse; note that the signal induced by the sensor has positive polarity. (b) Zoom-in of the pulse undershoot on a logarithmic time axis. The green line represents an exponential decay.

3 Results and discussion

3.1 Experimental results

Figure 4 a shows the measured ToT_1 (blue dots) from LED 1 and ToT_2 (orange triangles) from LED 2 as a function of the delay Δt between the two LEDs. The brightness was adjusted such that the set $\text{ToT}_1^{\text{true}} = 0.710 \mu\text{s}$ and set $\text{ToT}_2^{\text{true}} = 0.703 \mu\text{s}$, where ToT^{true} represents the corresponding unperturbed ToT. Furthermore, we set $I_{\text{Krum}} = 10$ steps. ToT_1 is constant ($\text{ToT}_1^{\text{true}}$) as a function of the delay whereas ToT_2 shows a much richer dynamics, and three distinct areas can be identified. In the first $\sim 1.1 \mu\text{s}$ (region 1, blue) a sharp drop of ToT_2 is observed. ToT_2 experiences a significant recovery over the next roughly $1.2 \mu\text{s}$ (region 2, red) and fully recovers within the following $\sim 10 \mu\text{s}$ to $\text{ToT}_2^{\text{true}}$ (region 3, green). The exponential recovery in the third region can be described by the model

$$\text{ToT}_2(\Delta t) = \text{ToT}_2^{\text{true}} (1 - B \exp(-\Delta t/\tau)) \quad (3.1)$$

with the recovering time τ and a fitting constant B . The green line in figure 4 a shows a fit to the data points with $\text{ToT}_2^{\text{true}} = 0.703 \mu\text{s}$, $B = 0.09$ and $\tau = 8.4 \mu\text{s}$.

Figure 4 b shows the recovery time τ from fitting the experimental data with (3.1) for a range of $\text{ToT}_1^{\text{true}}$ and $\text{ToT}_2^{\text{true}}$ combinations between 0.1 and $2 \mu\text{s}$. The recovery time is almost constant for all energy combinations, with a mean recovery time of $8.2 \mu\text{s}$ and a root-mean-square (RMS) deviation of $0.8 \mu\text{s}$.

The measured relative signal, $\text{ToT}_2/\text{ToT}_2^{\text{true}}$, at $\Delta t = 3 \mu\text{s}$ is shown in figure 5 a as a function of $\text{ToT}_1^{\text{true}}$ and $\text{ToT}_2^{\text{true}}$. A linear increase as a function of $\text{ToT}_1^{\text{true}}$ is observed for all $\text{ToT}_2^{\text{true}}$, which is

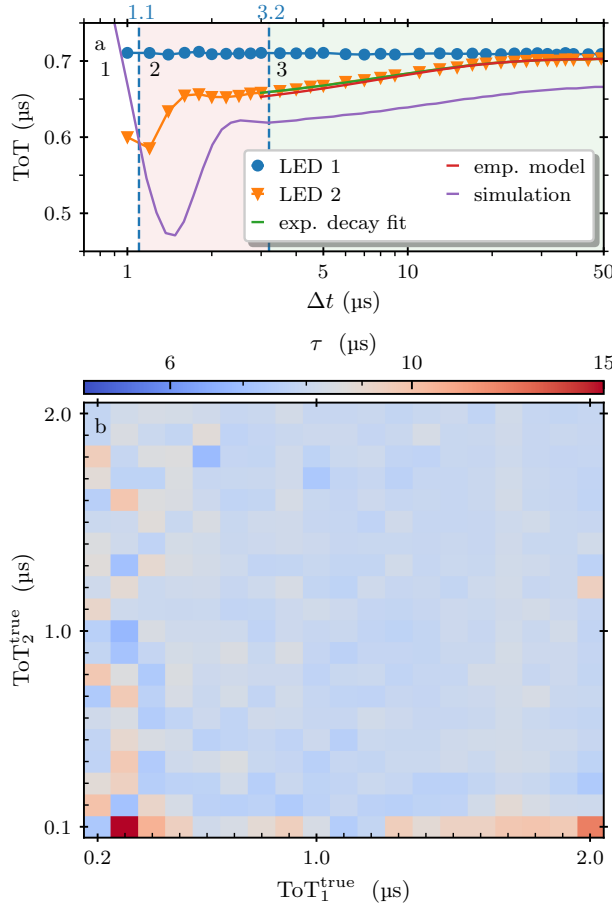


Figure 4. (a) Example measurement of ToT_1 and ToT_2 as a function of the relative delay. Moreover, we show the fit of the exponential decay model to ToT_2 according to (3.1) (green line), the results from an electronic-circuit simulation (purple line), and the results from the empirical model (red line). (b) Recovery times τ as a function of ToT_1^{true} and ToT_2^{true} obtained from the fits using (3.1); see text for details.

also depicted in figure 5 d for a selection of ToT_2^{true} -line outs. A larger slope is observed for smaller ToT_2^{true} values. The linearity of the relative signal as a function of ToT_1^{true} for all ToT_1^{true} - ToT_2^{true} combinations implies that the observed dynamics happens in the linear region of sensor operation and is not a saturation effect caused by the first LED pulse.

The relationship between the recovery time τ and I_{Krum} is illustrated in figure 6 as blue dots. Empirically, it was found that the recovery time was inversely proportional to I_{Krum} . The fitting model, described by $\tau = Q/I_{Krum}$ with $Q = (103.4 \mu s)(I_{Krum} \text{ step size}) = (103.4 \mu s) \cdot (0.24 \text{ nA}) = 24.8 \text{ fC}$, is represented by the green line. The reciprocal relationship between I_{Krum} and the recovery time implies that small changes in I_{Krum} at small I_{Krum} will result in a significant change in the recovery time, whereas the asymptotic slope is almost zero at higher I_{Krum} values, with $\tau = 0.41 \mu s$ at the maximum $I_{Krum} = 250$ steps.

3.2 Detector simulation

As depicted in figure 4 a, the variation of ToT_2 with Δt is closely related to the amplifier’s voltage response, and the non-equilibrium state of the amplifier upon arrival of the second pulse will affect

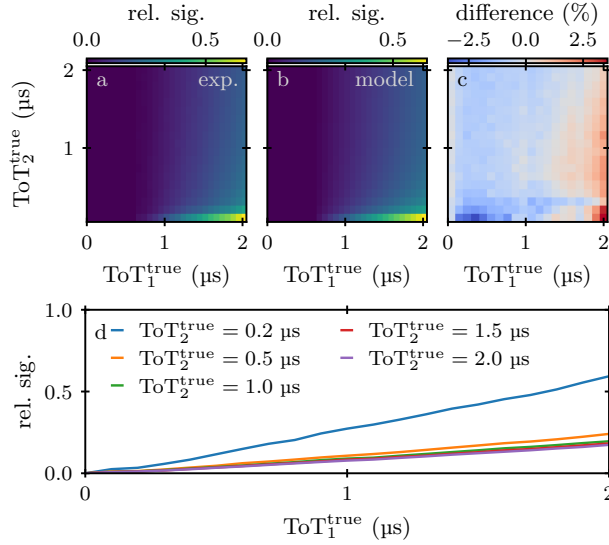


Figure 5. (a) Experimental relative signal at a fixed delay of 3 μs given by $ToT_2(\Delta t = 3 \mu s)/ToT_2^{true}$ from (3.1). (b) Relative signal extracted from the empirical model presented in section 3.3. (c) Difference of the data in (a) and (b). (d) Lines presenting values from selected rows in panel (a) to visualize the quasi-linear dependence of the relative signal on ToT_1^{true} .

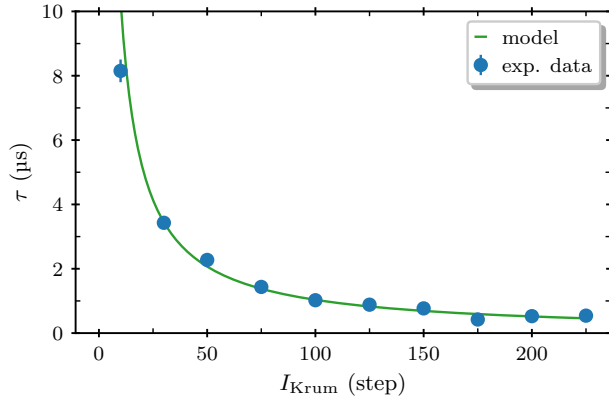


Figure 6. Dependency of the recovery time τ on I_{Krum} . The green line represents a weighted fit, $\tau = Q/I_{Krum}$ with $Q = 24.8 fC$, of the experimental data points with their standard error.

its measured ToT. The decrease in ToT_2 is due to two reasons, as depicted in figure 7. Firstly, the non-equilibrium state in region 3 results in a larger current on the input side and, therefore, an effective larger I_{Krum} . This is indicated by the steeper negative slope of the second event after the peak. Secondly, the shift in the voltage results in a reduced pulse height above the threshold. This explains the disproportionate reduction in signal observed when the second pulse is small, as seen in the bottom-right of figure 5 a. In summary, both effects result in a decreased ToT_2 in region 3.

Careful inspection of the simulation results shows good qualitative agreement regarding the slow recovery time extracted from the experiment. This can be explained by considering two components: the capacitor C_{Leak} and the transistor M_{Leak} in the leakage current compensation circuit. The temporary increase in leakage current compensation due to an incoming pulse is due to a charge increase on the capacitor C_{Leak} , which leads to a higher M_{Leak} transistor gate voltage, increasing its current. This

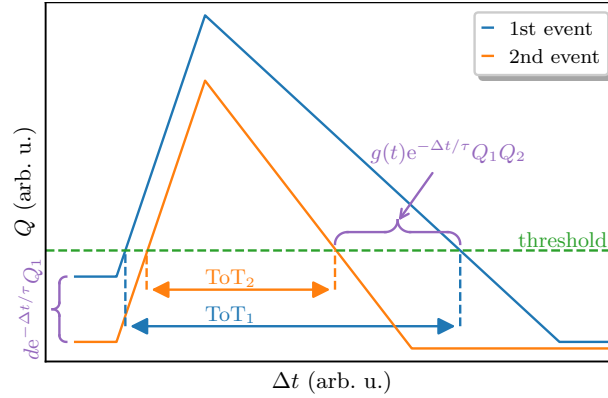


Figure 7. Illustration of the contributions for the presented loss model. Q_1 and Q_2 are directly proportional to ToT_1 and ToT_2 , respectively.

increased current in the transistor in turn causes the capacitor to discharge, resulting in an exponential decay to the baseline. The associated time constant is given by

$$\tau_{\text{Leak}} = \frac{C_{\text{Leak}}}{g_{mM_{\text{Leak}}}}, \quad (3.2)$$

where $g_{mM_{\text{Leak}}}$ is the small-signal transconductance of the transistor M_{Leak} . Given the values $C_{\text{Leak}} \sim 350$ fF and $g_{mM_{\text{Leak}}} = 24.5$ nS (for $I_{K_{\text{rum}}} = 1.5$ nA), this results in a time constant of $\tau_{\text{Leak}} = 14.3$ μ s, which is close to the experimentally observed recovery time. A qualitative sketch of the above described behaviour is provided in figure S3. As shown by (3.2), the time constant is inversely proportional to the transconductance of the leakage current compensation transistor M_{Leak} . Experimentally, the time constant is inversely proportional to $I_{K_{\text{rum}}}$, as shown in figure 6, which implies that the transconductance increases linearly with $I_{K_{\text{rum}}}$. This is consistent with simulation; the transistor is being operated in weak inversion, and under these conditions, the transconductance is proportional to the current.

So far, we have discussed region 3 of the amplifier and the ToT response, both corresponding to timescales longer than 3.2 μ s. To account for the full temporal behaviour, we consider a circuit analysis using the Laplace transform of the circuit’s transfer function. Points where the Laplace transform tends to infinity are called “poles”, and correspond to characteristic responses of the circuit, consisting generally of exponential responses, sinusoidal oscillations, or a combination of these (e.g. damped oscillations). The circuit contains five reactive elements (five capacitors) as depicted in figure 2. There are, however, only four independent initial conditions for these elements because capacitors C_{DET} , C_{FBK} , and C_{OUT} form a loop in which setting the initial conditions on two of them fixes the state of the third one. This leads to a system with four poles, which are on the left half plane, i.e., they correspond to either exponential decays or damped oscillations. One of these four poles corresponds to the long exponential undershoot in region 3 already discussed above. A second one corresponds to the rising amplifier pulse. Further detailed analysis of the circuit shows that, depending on the choice of the dimensions of the transistors in the front-end and also on the parasitic capacitances that are present in the circuit layout, the remaining two poles in the transfer function can be a pair of complex conjugate poles, corresponding to a damped sinusoidal oscillation in the time domain. These poles produce the pronounced damped oscillation of the time waveform signal in region 2.

Therefore, in region 2, a greater loss of the second pulse's ToT is observed than expected from the exponential decay alone, due to the sinusoidal undershoot suppressing the signal level. Finally, at very short times below $\Delta t = 1.1 \mu\text{s}$, when decreasing the delay time further, the second pulse piles up on the first pulse, extending the pulse duration and increasing the ToT. Decreasing the delay time even further leads to a scenario when the two pulses cannot be distinguished as separate events at the input of the discriminator, as explained in figure 1 a–b.

The observed effect is intrinsic to this kind of amplifier design, but delicately depends on the exact values of the used components and details of the circuit design used for the amplifier. We also confirmed the behaviour with a different chip and multiple pixels, showing the overall same characteristic with slightly different fitting constants. For example, as shown in figure S2, for another camera with an $I_{\text{Krumm}} = 10$, the recovery time was $\tau \sim 4.5 \mu\text{s}$ with a width of $0.4 \mu\text{s}$. We attribute these seemingly different results to the fact that the I_{Krumm} value is not an absolute calibrated value across multiple sensors, but varies from chip to chip.

3.3 Loss model

To predict the expected reduction in ToT_2 following an earlier illumination event with ToT_1 within delays observed in region 3, we developed an empirical mathematical model. Creating a model that encompasses the more complex dynamics of regions 1 and 2 is outside the scope of this work; see elsewhere for detailed numerical detector simulations [33]. We assume that the decrease of ToT_2 was primarily influenced by two effects: (1) due to increased leakage compensation a faster discharge of C_{FBK} is obtained and (2) due to the too high discharge of C_{FBK} the voltage level at which the second pulse starts off is lower than in the equilibrium level as illustrated in figure 3. With this, the relative loss $r(\Delta t)$ can be modelled in first order as:

$$\begin{aligned} r(\Delta t) &= 1 - \frac{\text{ToT}_2(\Delta t)}{\text{ToT}_2^{\text{true}}} \\ &\approx \text{ToT}_1^{\text{true}} e^{-\Delta t/\tau_m} \left(\frac{d}{\text{ToT}_2^{\text{true}} - t_{\text{ret}}} + g \right). \end{aligned} \quad (3.3)$$

Here, $\text{ToT}_2(\Delta t)$ is the measured amplitude of the second event at the time Δt , which is the time between the first and second hit in microseconds. The first and second pulse energies, proportional to $\text{ToT}_1^{\text{true}}$ and $\text{ToT}_2^{\text{true}}$, are denoted in microseconds. The fitting parameter τ_m represents the recovery time in microseconds, d is used to describe an offset between the equilibrium leakage compensation and the one due to a higher discharge, t_{ret} is an empirical parameter to improve the fit and g represents the factor responsible for the increased slope from a faster discharge due to higher leakage compensation. The good agreement between model and experimental data can also be observed in figure 4 a indicated by the red line. See the corresponding section S4 in the Supplementary data for more details.

Applying the model to the data presented, we list the parameters as follows: $\tau_m = 8.03 \mu\text{s}$, $d = 0.019$, $t_{\text{ret}} = 0.136 \mu\text{s}$, $g = 0.112 \mu\text{s}^{-1}$. The model's recovery time closely aligns with the experimental recovery time of $\tau = 8.01 \mu\text{s}$, as seen in figure 4 b. Due to t_{ret} in the denominator, the model only works for values greater than t_{ret} . Moreover, we note that due to variations in fabrication, the value of these parameters will vary somewhat between different Timepix3 chips, cf. our corresponding experimental findings above.

To further illustrate the strong agreement between our model and experimental data, figure 5 c depicts the difference between the model's results outlined in figure 5 b from (3.3) and the actual

experimental measurements in figure 5 a at $\Delta t = 3 \mu\text{s}$. Notably, the maximum relative difference between the model and the experimental data is merely $\pm 3.5\%$, and this variation is most pronounced for the lowest ToT_2 . The deviation is attributed to the simplicity of the model. Comparing figure 5 a and figure 5 b, this model provides a precise correction of the measured ToT , consequently improving the time resolution and the energy RMS [19, 26].

To obtain this calibration for a given Timepix3 assembly, it is beneficial to record more points for smaller ToT_2 s, whereas for $\text{ToT}_2 \gtrsim 0.7 \mu\text{s}$ this is not as critical any more. For our data, we found it sufficient to measure ToT_2 in the range $0.1 \dots 0.5 \mu\text{s}$ in increments of $0.1 \mu\text{s}$ and at $1, 1.5, 2 \mu\text{s}$ to obtain a very good fit.

The real $\text{ToT}_2^{\text{true}}$ can be obtained from the measured ToT_2 and ToT_1 by solving (3.3) for ToT_2 . However, an easier way is to use the relative loss directly:

$$\text{ToT}_2^{\text{true}} = \frac{\text{ToT}_2(\Delta t)}{1 - r(\Delta t)}. \quad (3.4)$$

4 Conclusions

Timepix3 based detectors not only enable precise nanosecond-level event timing, but also offer valuable deposited-energy information, crucial for a wide range of applications and essential for mitigating timewalk inaccuracies in time measurements. We found a systematic underestimation of event energy for events registered within $\sim 10 \mu\text{s}$ after previous events in the same pixel. For delays exceeding $2 \mu\text{s}$, this effect diminished exponentially, with the time constant inversely proportional to I_{Krum} . Our comprehensive analysis, utilizing integrating circuit design and simulations, is in very good agreement with the experimental observations.

Additionally, we introduce an empirical model to quantitatively assess the relative loss in the second event when the time interval between the first and second event exceeds approximately $3 \mu\text{s}$. This model demonstrates exceptional alignment with experimental data and offers the potential for real-time post-processing correction of ToT losses. The implementation of such correction measures holds the promise of improving experimental data, thereby enhancing our proficiency in sub-pixel positioning, timewalk correction, and related applications.

Overall, our findings not only advance our understanding of Timepix3's capabilities, but also provide clear practical means to optimize the detector's performance for a wide range of applications that benefit from improved time resolution and precise event-energy measurements. In similar detectors like Medipix3 and Timepix4, the described effect is either not present or reduced due to a different functionality or amplifier design, respectively. In future developments, it is envisioned to eliminate this loss fully.

Code and data availability. The dataset and the analysis code are available in a Jupyter notebook and are provided by the authors upon reasonable request.

Acknowledgments

We gratefully acknowledge Guido Meier for initial discussions of our findings and the DESY Nanolab for experimental support. We thank Amsterdam Scientific Instruments B. V. for collaborative exchange.

We acknowledge financial support by Deutsches Elektronen-Synchrotron DESY, a member of the Helmholtz Association (HGF), also for the provision of experimental facilities and for the use of the Maxwell computational resources operated at DESY. We acknowledge support by the Matter innovation pool of the Helmholtz Association through the DataX project. The research was further supported by the Cluster of Excellence “Advanced Imaging of Matter” (AIM, EXC 2056, ID 390715994) of the Deutsche Forschungsgemeinschaft (DFG).

References

- [1] M. Garcia-Sciveres and N. Wermes, *A review of advances in pixel detectors for experiments with high rate and radiation*, *Rept. Prog. Phys.* **81** (2018) 066101 [[arXiv:1705.10150](#)].
- [2] N. Wermes, *Pixel detectors ... where do we stand?*, *Nucl. Instrum. Meth. A* **924** (2019) 44 [[arXiv:1804.10640](#)].
- [3] C. Ponchut, N. Tartoni and D. Pennicard, *X-ray imaging at synchrotron research facilities*, *Radiat. Meas.* **140** (2021) 106459.
- [4] E.H.M. Heijne, *History and future of radiation imaging with single quantum processing pixel detectors*, *Radiat. Meas.* **140** (2021) 106436.
- [5] R. Ballabriga, M. Campbell and X. Llopert, *Asic developments for radiation imaging applications: The medipix and timepix family*, *Nucl. Instrum. Meth. A* **878** (2018) 10.
- [6] P. Delpierre, *A history of hybrid pixel detectors, from high energy physics to medical imaging*, *2014 JINST* **9** C05059.
- [7] R. Ballabriga et al., *The Timepix4 analog front-end design: Lessons learnt on fundamental limits to noise and time resolution in highly segmented hybrid pixel detectors*, *Nucl. Instrum. Meth. A* **1045** (2023) 167489.
- [8] S. Procz et al., *X-ray and gamma imaging with Medipix and Timepix detectors in medical research*, *Radiat. Meas.* **127** (2019) 106104.
- [9] R. Al Darwish, L. Marcu and E. Bezak, *Overview of current applications of the Timepix detector in spectroscopy, radiation and medical physics*, *Applied Spectroscopy Reviews* **55** (2019) 243.
- [10] C. Cheng et al., *3D velocity map imaging of electrons with TPX3CAM*, *Rev. Sci. Instrum.* **93** (2022) 013003.
- [11] J. Unwin et al., *X-ray induced Coulomb explosion imaging of transient excited-state structural rearrangements in CS₂*, *Commun. Phys.* **6** (2023) 309.
- [12] M.N.R. Ashfold et al., *Imaging the dynamics of gas phase reactions*, *Phys. Chem. Chem. Phys.* **8** (2006) 26.
- [13] A.I. Chichinin, K.-H. Gericke, S. Kauczok and C. Maul, *Imaging chemical reactions — 3D velocity mapping*, *Int. Rev. Phys. Chem.* **28** (2009) 607.
- [14] H. Paganetti, *Proton Beam Therapy*, in *Proton Beam Therapy*, IOP Publishing (2016) [[DOI:10.1088/978-0-7503-1370-4ch1](#)].
- [15] R. Aaij et al., *Performance of the LHCb Vertex Locator*, *2014 JINST* **9** P09007 [[arXiv:1405.7808](#)].
- [16] K. Akiba et al., *The Timepix Telescope for High Performance Particle Tracking*, *Nucl. Instrum. Meth. A* **723** (2013) 47 [[arXiv:1304.5175](#)].
- [17] B. Bergmann, P. Burian, P. Manek and S. Pospisil, *3D reconstruction of particle tracks in a 2 mm thick CdTe hybrid pixel detector*, *Eur. Phys. J. C* **79** (2019) 165.

- [18] R. Filgas et al., *RISEPix — A Timepix-based radiation monitor telescope onboard the RISESAT satellite*, *Astron. Nachr.* **340** (2019) 674.
- [19] H. Bromberger et al., *Shot-by-shot 250 kHz 3D ion and MHz photoelectron imaging using Timepix3*, *J. Phys. B* **55** (2022) 144001 [[arXiv:2111.14407](#)].
- [20] A. Kruth et al., *Timepix3: a 65K channel hybrid pixel readout chip with simultaneous ToA/ToT and sparse readout*, 2014 *JINST* **9** C05013.
- [21] X. Llopart et al., *Timepix, a 65k programmable pixel readout chip for arrival time, energy and/or photon counting measurements*, *Nucl. Instrum. Meth. A* **581** (2007) 485.
- [22] X. Llopart et al., *Timepix4, a large area pixel detector readout chip which can be tiled on 4 sides providing sub-200 ps timestamp binning*, 2022 *JINST* **17** C01044.
- [23] K. Heijhoff et al., *Timing measurements with a 3D silicon sensor on Timepix3 in a 180 hadron beam*, 2021 *JINST* **16** P08009 [[arXiv:2105.11800](#)].
- [24] M. Fisher-Levine and A. Nomerotski, *TimepixCam: a fast optical imager with time-stamping*, 2016 *JINST* **11** C03016.
- [25] A. Roberts et al., *First demonstration of 3D optical readout of a TPC using a single photon sensitive Timepix3 based camera*, 2019 *JINST* **14** P06001 [[arXiv:1810.09955](#)].
- [26] F. Pitters et al., *Time resolution studies of Timepix3 assemblies with thin silicon pixel sensors*, 2019 *JINST* **14** P05022 [[arXiv:1901.07007](#)].
- [27] B. van der Heijden et al., *SPIDR, a general-purpose readout system for pixel ASICs*, 2017 *JINST* **12** C02040.
- [28] A. Al-Refaie et al., *PymePix: A python library for SPIDR readout of Timepix3*, 2019 *JINST* **14** P10003 [[arXiv:1905.07999](#)].
- [29] CFEL Controlled Molecule Imaging, *PymePix*, Code repository, <https://gitlab.desy.de/CMI/CMI-public/pymepix> (2020).
- [30] Tango Controls, <https://www.tango-controls.org/about-us/> (2023).
- [31] F. Krummenacher, *Pixel detectors with local intelligence: an IC designer point of view*, *Nucl. Instrum. Meth. A* **305** (1991) 527.
- [32] C.D. Systems, *Cadence Virtuoso Studio*, https://www.cadence.com/en_US/home/tools/custom-ic-analog-rf-design/virtuoso-studio.html (2022).
- [33] R. Ballabriga Sune et al., *A simulator for Timepix-like pixel front-ends*, 2024 *JINST* **19** C03022.